Partial Parabolic Single Layer Crossing for Silicon-on-Insulator Nanophotonic Waveguides

Yuan-Ting Shih, Kuo-Fang Chung, and Ding-Wei Huang, *Member, IEEE*

***Abstract*—Under the dimension of 6 μm overall length, a 220 nm partial parabolic taper fabricated on silicon-on-insulator (SOI) wafer with 2 μm buried oxide at 1.55 μm, to simply fabrication processes and reduce cost, we design a Partial parabolic single layer crossing, which modifies crossing curves around the crossing regions and input-output regions of crossing for fitting the initial input status of the fundamental mode. This single layer crossing for SOI photonic wires which are broadened using a 3 μm partial parabolic taper in each arm to get 97.8% high transmission (−0.097 dB) and −62 dB low crosstalk. It not only can simplify the fabrication processes, reduce cost, and shrink device size to produce more compact photonic circuits, but also keep high transmission over 96.8% even under ±10 nm fabrication dimension variation.**

***Index Terms*—Integrated nanophotonic, waveguide devices.**

I. Introduction

THE concept of optical integrated circuits (OICs) was introduced in the end of 1960 for optical communication, signal processing, optical computing and sensing. OICs was designed to have a certain function by integrating a source (laser diode), functional components (switches, modulators), interconnection waveguides and detectors (photo diodes) on a single substrate [1]. The development of optical and electrical packaging integrated optical I/O directly with electronic circuits (electrical packages with optical I/O and optical waveguide-based printed circuit boards). It heavily influenced the associated cost of systems cabling, power dissipation of the link and system cooling etc. [2]. In the late of 1980s, the silicon photonics started to develop, then in the late 1990s its technology booming and abundance of the private capital triggered a rapid growth. Owing to the strong optical confinement of high index contrast between silicon ($n = 3.455$) and SiO_2 ($n = 1.45$) scaling photonic devices wafers to nanometer level, silicon photonics researchers created low-cost photonics (waveguide circuits) on silicon-on-insulator (SOI) with the mighty IC industry for mass-market applications. It also provided a solution to solve the thermal and cooling problems of system [3]. From 2004, investments of industry and government quickened the pace of the development of silicon photonics and brought out preliminary results which indicated that the silicon photonics were truly CMOS compatible, however, silicon laser had not been attained [4]. In 2006, a low-cost hybrid silicon laser was created and can be performed at the wafer or die level to provide a solution for large-scale optical integration onto a silicon platform. This development solved one of the last obstacles of integrated silicon photonics to produce low-cost, highly integrated silicon photonic chips [5]. Silicon photonics were created by a laser source manufactured directly on the silicon photonic chip. High-transmission, low-loss, low-crosstalk, and low-cost waveguides crossing of silicon-on-insulator (SOI) photonic wires was one of critical important fundamental components for producing dense and compact silicon photonic circuits. It was one of good solutions to solve interconnections problems of SOI photonic circuits. There were many kinds of waveguide crossings designed out, such as direct, elliptical, parabolic, etc. modes, including single, double and multi-layers [6]–[12].

Especially, W. Bogaerts etc. presented a double layer parabolic taper crossing of 6 μm overall length which was constituted of a shallow-etched parabolic taper etched through the 220 nm silicon core fabricated top over 2 μm oxide on SOI photonic wires. To reduce the diffraction losses in the crossing region, they introduced a scheme to maintain confinement over a larger part of the expanded crossing, which at the same time lowered the lateral refractive index contrast. The lower index contrast reduced the diffraction and back reflections in the nonconfined region. The lower lateral index contrast of the waveguide was achieved through a double-etch scheme. The high-contrast photonic wires and the parabolic mode expanders were etched through the silicon core, but a shallow-etched crossing confined the light to the center of the mode expander. The crossing had a parabolic expander would reach a center width of 2.5 μm. The shallow-etched waveguide expanded linearly from 0.5 to 0.8 μm over the length of the crossing, and each 3 μm parabolic taper with a lower index contrast using a double-etch technique crossing to reduce the diffraction losses in the crossing region, details as Fig. 1. At the wavelength of 1.55 μm, its transmission is over 95%. When the start of shallow etch at left of the starting position of the fundamental mode input (< -3 μm), the transmission raises up to over 97.5% [13].

II. Design and Simulations

Under the same dimension of 6 μm overall length, a shallow-etched parabolic taper etched through the 220 nm

Manuscript received December 30, 2021; revised February 12, 2022; accepted February 16, 2022. Date of publication February 22, 2022; date of current version March 11, 2022. This work was supported by the Ministry of Science and Technology, Taiwan under Grant MOST 110-2224-E-992-001. *(Corresponding author: Ding-Wei Huang.)*

Yuan-Ting Shih and Kuo-Fang Chung are with the Graduate Institute of Photonics and Optoelectronics, National Taiwan University, Taipei 106319, Taiwan (e-mail: d03941012@ntu.edu.tw; d08941008@ntu.edu.tw).

Ding-Wei Huang is with the Department of Electrical Engineering and the Graduate Institute of Photonics and Optoelectronics, National Taiwan University, Taipei 106319, Taiwan (e-mail: dwhuang@ntu.edu.tw).

Digital Object Identifier 10.1109/JPHOT.2022.3152923

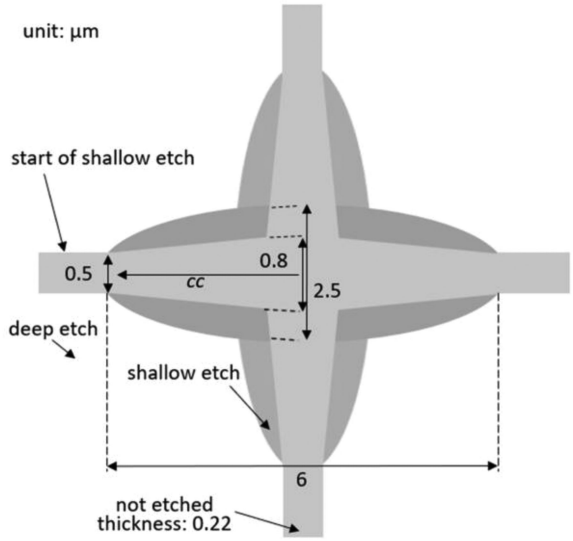

Fig. 1. Double layer parabolic taper crossing.

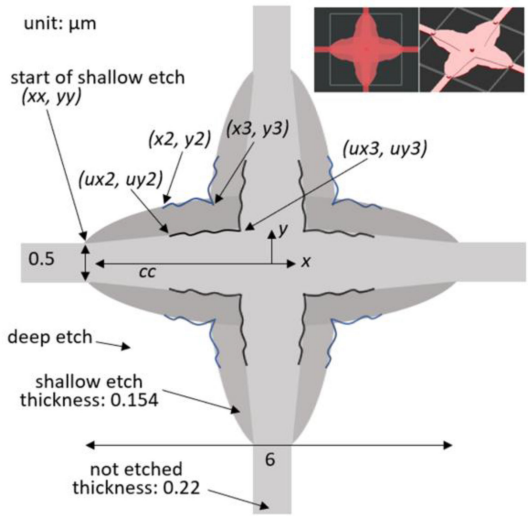

Fig. 2. Double layer parabolic taper crossing with modifying crossing curves around the upper and lower crossing regions.

silicon core fabricated over 2 μm buried oxide of SOI wafer at the wavelength of 1.55 μm, to reduce the diffraction losses more in the crossing region, we modify crossing curves around the upper and lower crossing regions, details as shown in Fig. 2. When the start of shallow etch at the starting position of the fundamental mode input ($xx = -3$ μm, $yy = 0.25$ μm) and parabola focus $cc = -2.90$ μm, using finite-difference time-domain (FDTD) simulation [14]–[16] and particle swarm optimization (PSO) method [17]–[20], we got a good result of transmission 97.7% and its electric (E) field distribution as shown in Fig. 3, where transmission is calculated at output of crossing by the optimization figure of merit (FOM) which is transmission(T) minus back reflection(R) and 2× crosstalk.

$$\text{Transmission } (\%) = \text{FOM} = T - R - 2 \times \text{crosstalk} \quad (1)$$

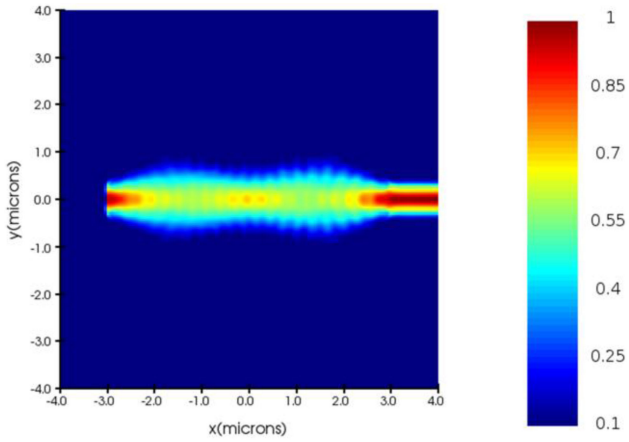

Fig. 3. E field distribution of double layer parabolic taper crossing with modifying crossing curves around the upper and lower crossing regions.

TABLE I
SEGMENTATION LEVELS BETWEEN ($x2$, $y2$) AND ($x3$, $y3$)

Level 1 2^1 segments by ($x\_\{xi\}$, $y\_\{xi\}$); i = 1,9,17	($x\_\{x1\}$, $y\_\{x1\}$), ($x\_\{x9\}$, $y\_\{x9\}$), ($x\_\{x17\}$, $y\_\{x17\}$); where ($x\_\{x1\}$, $y\_\{x1\}$) = ($x2$, $y2$), ($x\_\{x17\}$, $y\_\{x17\}$) = ($x3$, $y3$).
Level 2 2^2 segments by ($x\_\{xi\}$, $y\_\{xi\}$); i = 1,5,9,13,17	($x\_\{x1\}$, $y\_\{x1\}$), ($x\_\{x5\}$, $y\_\{x5\}$), ($x\_\{x9\}$, $y\_\{x9\}$), ($x\_\{x13\}$, $y\_\{x13\}$), ($x\_\{x17\}$, $y\_\{x17\}$)
Level 3 2^3 segments by ($x\_\{xi\}$, $y\_\{xi\}$); i = 1,3,5,7,9,11,13,15,17	($x\_\{x1\}$, $y\_\{x1\}$), ($x\_\{x3\}$, $y\_\{x3\}$), ($x\_\{x5\}$, $y\_\{x5\}$), ($x\_\{x7\}$, $y\_\{x7\}$), ($x\_\{x9\}$, $y\_\{x9\}$), ($x\_\{x11\}$, $y\_\{x11\}$), ($x\_\{x13\}$, $y\_\{x13\}$), ($x\_\{x15\}$, $y\_\{x15\}$), ($x\_\{x17\}$, $y\_\{x17\}$)
Level 4 2^4 segments by ($x\_\{xi\}$, $y\_\{xi\}$); i = 1,2,3,4,5,6,7,8,9,10,11, 12,13,14,15,16,17	($x\_\{x1\}$, $y\_\{x1\}$), ($x\_\{x2\}$, $y\_\{x2\}$), ($x\_\{x3\}$, $y\_\{x3\}$), ($x\_\{x4\}$, $y\_\{x4\}$), ($x\_\{x5\}$, $y\_\{x5\}$), ($x\_\{x6\}$, $y\_\{x6\}$), ($x\_\{x7\}$, $y\_\{x7\}$), ($x\_\{x8\}$, $y\_\{x8\}$), ($x\_\{x9\}$, $y\_\{x9\}$), ($x\_\{x10\}$, $y\_\{x10\}$), ($x\_\{x11\}$, $y\_\{x11\}$), ($x\_\{x12\}$, $y\_\{x12\}$), ($x\_\{x13\}$, $y\_\{x13\}$), ($x\_\{x14\}$, $y\_\{x14\}$), ($x\_\{x15\}$, $y\_\{x15\}$), ($x\_\{x16\}$, $y\_\{x16\}$), ($x\_\{x17\}$, $y\_\{x17\}$)

The segmented structures are based on the bisection method [21], and we design 4 levels to find 17 segmentation points for dividing the design into 16 segments. As Tables I–III, on Level 1 we find segmentation points: Nos. 1, 9, and 17 for processing 2^1 segments. On Level 2, based on segmentation points: Nos. 1, 9, and 17, we find segmentation points: Nos. 5 and 13 for processing 2^2 segments. On Level 3, based on segmentation points: Nos. 1, 5, 9, 13, and 17, we find segmentation points: Nos. 3, 7, 11, and 15 for processing 2^3 segments. On Level 4, based on segmentation points: Nos. 1, 3, 5, 7, 9, 11, 13, 15, and 17, we find segmentation points: Nos. 2, 4, 6, 8, 10, 12, 14, and 16 for processing 2^4 segments. Between ($x2$, $y2$) and ($x3$, $y3$), we set 4 segmentation levels for fitting new curves, the details as shown in Table I. Between ($ux2$, $uy2$) and ($ux3$, $uy3$), we also set 4 segmentation levels as shown in Table II. The flow chart of the double-layer simulation processes is shown in Fig. 4. We get the high FOM 97.8% of Figs. 2 and 3. at Level 3, its parameters as bellows: ($x\_\{x1\}$, $y\_\{x1\}$) = ($x2$, $y2$) = (−1.9798, 0.9033), ($x\_\{x3\}$, $y\_\{x3\}$)

TABLE II
SEGMENTATION LEVELS BETWEEN (*ux*2, *uy*2) AND (*ux*3, *uy*3)

Level 1 2^1 segments by (x_{ui}, y_{ui}); i = 1,9,17	(x_{u1}, y_{u1}), (x_{u9}, y_{u9}), (x_{u17}, y_{u17}); where (x_{u1}, y_{u1}) = (*ux2, uy2*), (x_{u17}, y_{u17}) = (*ux3, uy3*).
Level 2 2^2 segments by (x_{ui}, y_{ui}); i = 1,5,9,13,17	(x_{u1}, y_{u1}), (x_{u5}, y_{u5}), (x_{u9}, y_{u9}), (x_{u13}, y_{u13}), (x_{u17}, y_{u17})
Level 3 2^3 segments by (x_{ui}, y_{ui}); i = 1,3,5,7,9,11,13,15,17	(x_{u1}, y_{u1}), (x_{u3}, y_{u3}), (x_{u5}, y_{u5}), (x_{u7}, y_{u7}), (x_{u9}, y_{u9}), (x_{u11}, y_{u11}), (x_{u13}, y_{u13}), (x_{u15}, y_{u15}), (x_{u17}, y_{u17})
Level 4 2^4 segments by (x_{ui}, y_{ui}); i = 1,2,3,4,5,6,7,8,9,10,11, 12,13,14,15,16,17	(x_{u1}, y_{u1}), (x_{u2}, y_{u2}), (x_{u3}, y_{u3}), (x_{u4}, y_{u4}), (x_{u5}, y_{u5}), (x_{u6}, y_{u6}), (x_{u7}, y_{u7}), (x_{u8}, y_{u8}), (x_{u9}, y_{u9}), (x_{u10}, y_{u10}), (x_{u11}, y_{u11}), (x_{u12}, y_{u12}), (x_{u13}, y_{u13}), (x_{u14}, y_{u14}), (x_{u15}, y_{u15}), (x_{u16}, y_{u16}), (x_{u17}, y_{u17})

TABLE III
SEGMENTATION LEVELS BETWEEN (*xx*, *yy*) AND (*x*1, *y*1)

Level 1 2^1 segments by (x_{si}, y_{si}); i = 1,9,17	(x_{s1}, y_{s1}), (x_{s9}, y_{s9}), (x_{s17}, y_{s17}); where (x_{s1}, y_{s1}) = (*xx, yy*), (x_{s17}, y_{s17}) = (*x1, y1*).
Level 2 2^2 segments by (x_{si}, y_{si}); i = 1,5,9,13,17	(x_{s1}, y_{s1}), (x_{s5}, y_{s5}), (x_{s9}, y_{s9}), (x_{s13}, y_{s13}), (x_{s17}, y_{s17})
Level 3 2^3 segments by (x_{si}, y_{si}); i = 1,3,5,7,9,11,13,15,17	(x_{s1}, y_{s1}), (x_{s3}, y_{s3}), (x_{s5}, y_{s5}), (x_{s7}, y_{s7}), (x_{s9}, y_{s9}), (x_{s11}, y_{s11}), (x_{s13}, y_{s13}), (x_{s15}, y_{s15}), (x_{s17}, y_{s17})
Level 4 2^4 segments by (x_{si}, y_{si}); i = 1,2,3,4,5,6,7,8,9,10,11, 12,13,14,15,16,17	(x_{s1}, y_{s1}), (x_{s2}, y_{s2}), (x_{s3}, y_{s3}), (x_{s4}, y_{s4}), (x_{s5}, y_{s5}), (x_{s6}, y_{s6}), (x_{s7}, y_{s7}), (x_{s8}, y_{s8}), (x_{s9}, y_{s9}), (x_{s10}, y_{s10}), (x_{s11}, y_{s11}), (x_{s12}, y_{s12}), (x_{s13}, y_{s13}), (x_{s14}, y_{s14}), (x_{s15}, y_{s15}), (x_{s16}, y_{s16}), (x_{s17}, y_{s17})

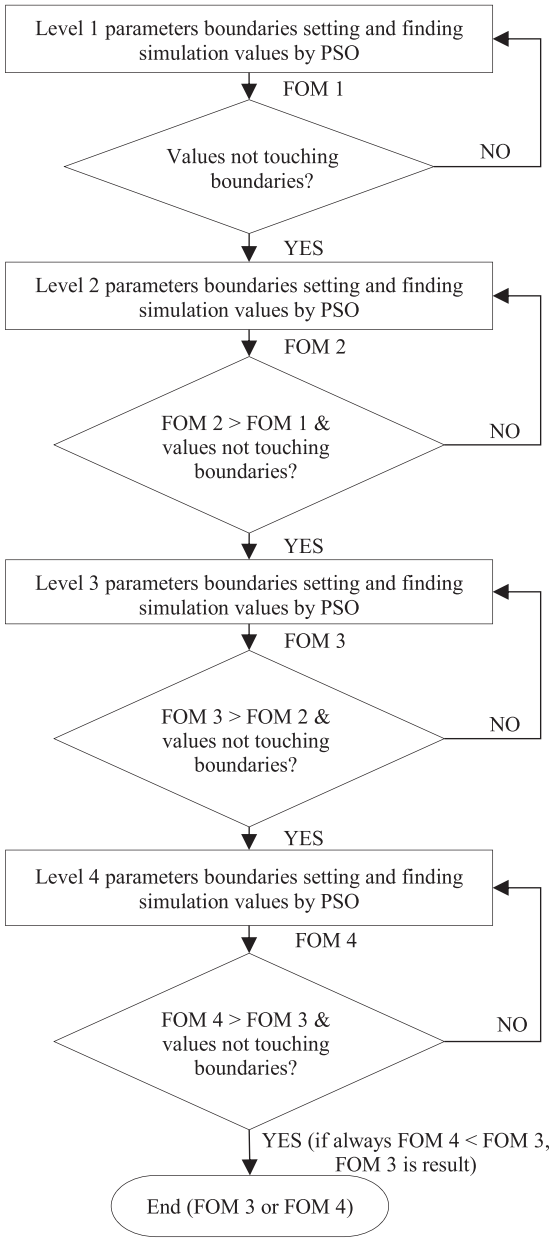

Fig. 4. Flow chart of simulation process.

= (−1.9768, 0.9328), (x_{x5}, y_{x5}) = (−1.9314, 0.8749), (x_{x7}, y_{x7}) = (−1.9300, 0.8997), (x_{x9}, y_{x9}) = (−1.8838, 0.8465), (x_{x11}, y_{x11}) = (−1.7114, 0.8473), (x_{x13}, y_{x13}) = (−1.5344, 0.8555), (x_{x15}, y_{x15}) = (−1.2103, 1.0748), (x_{x17}, y_{x17}) = (−1.0010, 1.0010); (x_{u1}, y_{u1}) = (*ux*2, *uy*2) = (−2.3308, 0.3514), (x_{u3}, y_{u3}) = (−1.7941, 0.3518), (x_{u5}, y_{u5}) = (−1.6242, 0.3991), (x_{u7}, y_{u7}) = (−1.3666, 0.4756), (x_{u9}, y_{u9}) = (−1.3212, 0.4639), (x_{u11}, y_{u11}) = (−1.2692, 0.4565), (x_{u13}, y_{u13}) = (−0.9747, 0.5121), (x_{u15}, y_{u15}) = (−0.6453, 0.55484), (x_{u17}, y_{u17}) = (*ux*3, *uy*3) = (−0.5406, 0.5406). Because of the complex structures of the 2-layer designs for reducing the diffraction losses in the crossing region, it's hard to find a trend in these parameters to provide physical explanation for the optimization results.

Under the same dimension of 6 μm overall length, a shallow-etched parabolic taper etched through the 220 nm silicon core fabricated over 2 μm buried oxide of SOI wafer at the wavelength of 1.55 μm, compared with parabolic taper without modifying crossing curves as shown in Fig. 5, when the start of shallow etch at the starting position of the fundamental mode input (−3 μm) and parabola focus *cc* at −2.90 μm, using FDTD and PSO results in a transmission 96.5%, and its *E* field distribution as shown in Fig. 6. Obviously, double layer parabolic taper crossing with modifying crossing curves around the upper and lower crossing regions result in a better effectiveness to reduce the diffraction losses in the crossing region than that without modifying crossing curves around the upper and lower crossing regions.

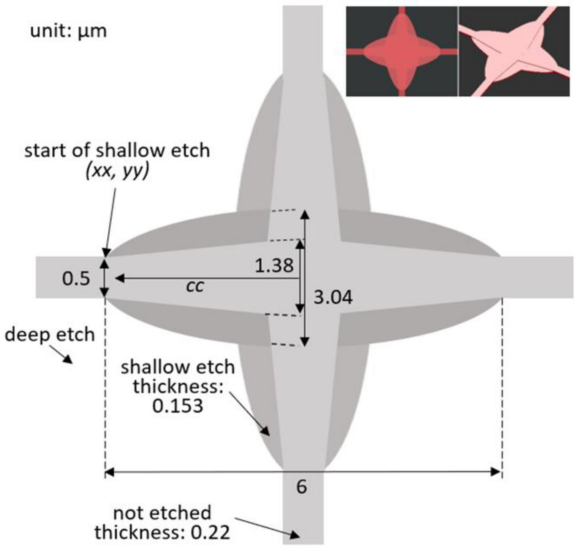

Fig. 5. Double layer parabolic taper crossing without modifying crossing curves around the upper and lower crossing regions.

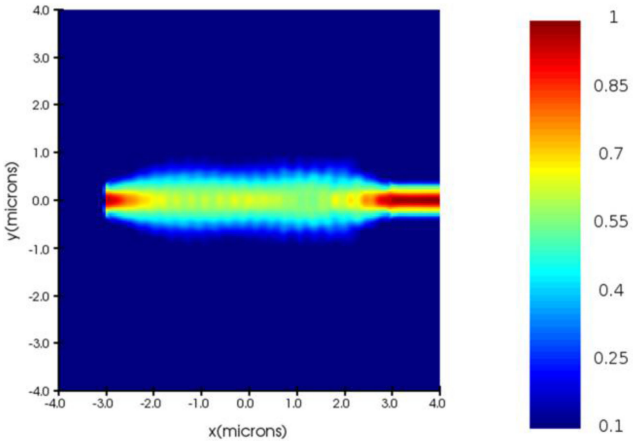

Fig. 6. *E* field distribution of double layer parabolic taper crossing without modifying crossing curves around the upper and lower crossing regions.

Under the dimension of 6 μm overall length, a 220 nm partial parabolic taper fabricated on SOI wafer with 2 μm buried oxide at 1.55 μm, to simply fabrication processes and reduce cost, we replace the upper crossing (not etched) regions of double layer parabolic taper crossing (Fig. 2) by designing a "partial parabolic single layer crossing" not only modifying crossing curves around the crossing regions but also modifying input and output regions of crossing for fitting the initial input status of the fundamental mode. Comparing with the double layer parabolic taper crossing structure, the single layer crossing was easier calculated by a mathematical model to estimate its structure parameters for achieving high transmission, details as shown in Fig. 7. At the beginning of the optimization process, the curve is parabola. After the optimization is completed, the perimeter of the curve deviates from the original parabola and becomes a wriggling curve so as to achieve a high transmission.

The positions of parabola focus and beam equivalent Gaussian waist are both the same at *cc* μm. Under the different numbers

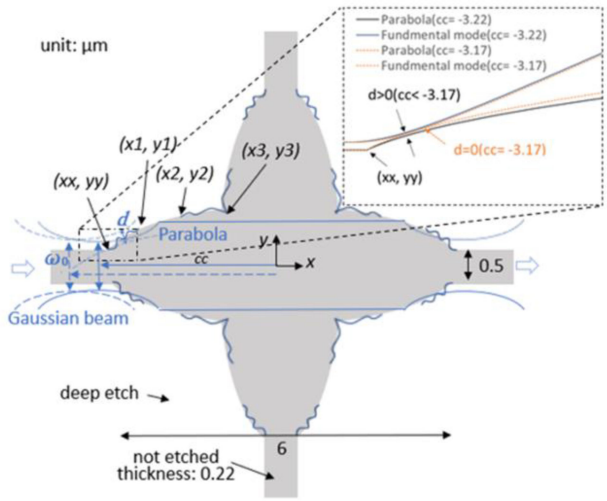

Fig. 7. Partial parabolic single layer crossing.

of *cc* μm, we get different curves of the fundamental mode and parabola, and there is a distance *d* μm between them (the blue solid and dashed lines in Fig. 7.). We obtain *d* from the function of the fundamental mode width y_ω (as a function of *x*, and its beam waist located at *cc*) and parabola function y_p as bellows:

$$y_\omega = \omega_0 \sqrt{1 + \left(\frac{\lambda\,(x - cc)}{n\pi {\omega_0}^2} \right)^2}, \tag{2}$$

$$y_{\mathrm{p}} = 2\sqrt{C_p\,(x - hh)}, \tag{3}$$

where ω_0 is the beam waist of the fundamental mode 0.34 μm, λ is wave length 1.55 μm, *n* is silicon refractive index 3.455, *cc* is the position of ω_0 and parabola focus. The parabola always passes through the point ($xx = -3$ μm, $yy = 0.25$ μm) which is the intersection of the input waveguide arm and the crossing with its shape determined by (*xx*, *yy*) and (*cc*,0), and C_p is the distance between parabola vertex *hh* and focus *cc*,

$$C_p = \frac{1}{2}\left((cc - xx) + \sqrt{(xx - cc)^2 + yy^2} \right), \tag{4}$$

where $xx = -3$ μm, $yy = 0.25$ μm and $hh = cc - C_p$. When $cc = -3.17$ μm, $x = -2.43$ μm, $y = y_\omega = y_p = 0.462$ μm, the fundamental mode and parabola are tangent each other. Around the position, *cc* from −3.22 to −3.16 μm, using FDTD and PSO we get curves parameters of high transmission more than 96.5% and from −3.20 to −3.19 μm, more than 97.5%, their relative information as shown in Fig. 8. One of the excellent examples shows a high transmission 97.8% (−0.097 dB) and low crosstalk −62 dB as shown in Fig. 9, its *E* field distribution as shown in Fig. 10.

Between (*x*2, *y*2) and (*x*3, *y*3), we set the same 4 segmentations levels for fitting new curve as shown in Table I. Between (*xx*, *yy*) and (*x*1, *y*1), we also set 4 segmentations as shown in Table III. The flow chart of the single-layer simulation processes is the same as that shown in Fig. 4. We get the high FOM 97.8% of Figs. 9 and 10 at Level 3, its parameters as bellows: (*x*_{*s*1}, *y*_{*s*1}) = (*xx*, *yy*) = (−3.00, 0.25), (*x*_{*s*3}, *y*_{s3})

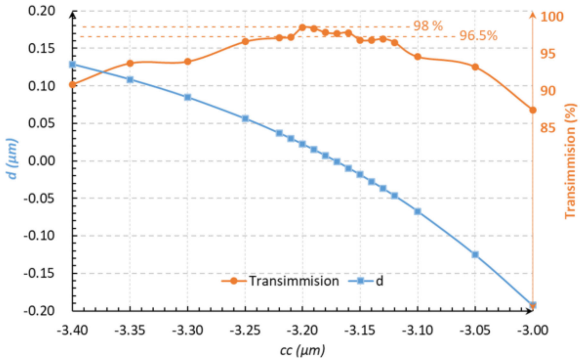

Fig. 8. High transmission ranges of partial parabolic single layer crossings.

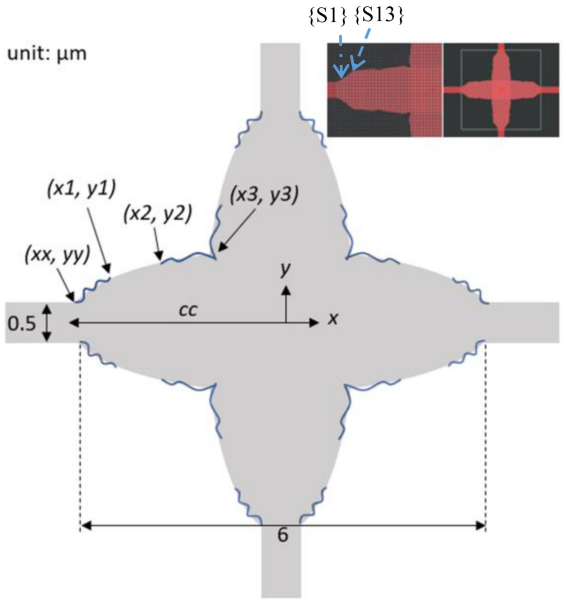

Fig. 9. One (transmission 97.8%) of excellent examples of partial parabolic single layer crossing.

= (−2.8711, 0.2859), (x_{s5}, y_{s5}) = (−2.7244, 0.3598), (x_{s7}, y_{s7}) = (−2.6705, 0.3873), (x_{s9}, y_{s9}) = (−2.6131, 0.4346), (x_{s11}, y_{s11}) = (−2.2578, 0.5481), (x_{s13}, y_{s13}) = (−2.0022, 0.5628), (x_{s15}, y_{s15}) = (−1.7443, 0.5606), (x_{s17}, y_{s17}) = (x1, y1) = (−1.70, 0.5457); (x_{x1}, y_{x1}) = (x2, y2) = (−1.35, 0.6010), (x_{x3}, y_{x3}) = (−1.2453, 0.6063), (x_{x5}, y_{x5}) = (−1.2368, 0.6074), (x_{x7}, y_{x7}) = (−0.9793, 0.6603), (x_{x9}, y_{x9}) = (−0.7263, 0.6459), (x_{x11}, y_{x11}) = (−0.7008, 0.6410), (x_{x13}, y_{x13}) = (−0.6814, 0.6339), (x_{x15}, y_{x15}) = (−0.6533, 0.6329), (x_{x17}, y_{x17}) = (x3, y3) = (−0.6372, 0.6372). Between {s1} and {s13}, the fitting curve is like a horn, as shown in Fig. 9, and it is useful to fit the initial input status of the fundamental mode for high transmission outputs.

The narrower crossing size can produce more compact photonic circuits to shrink the device size. The crossing size is mainly decided by parabola dimension, which is depend on its focus position *cc*. When $cc > -3$ μm (at right of the starting position of the fundamental mode input), parabola has wide

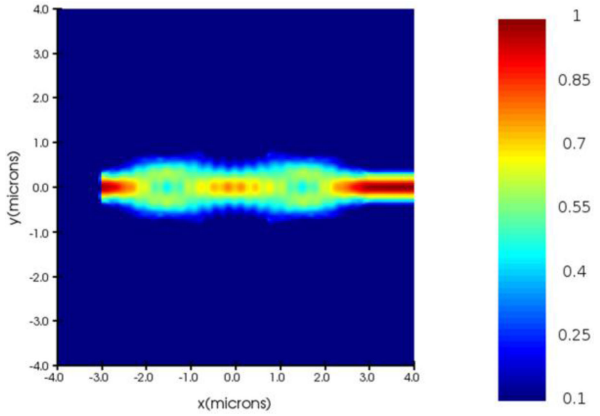

Fig. 10. *E* field distribution of the excellent example (transmission 97.8%) of partial parabolic single layer crossing.

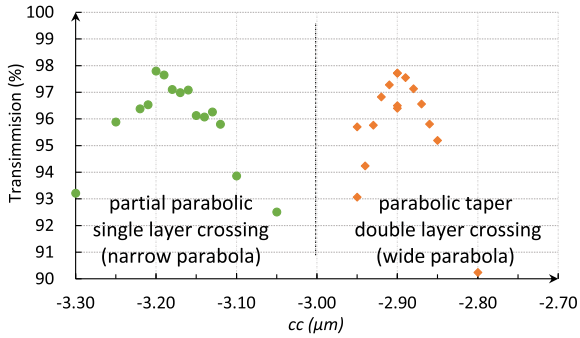

Fig. 11. Crossings dimension comparison.

dimension, but $cc < -3$ μm (at left of the starting position of the fundamental mode input) narrow. Comparing with parabolic taper double layer crossing, the *cc* of the partial parabolic single layer crossing < -3 μm has narrow parabola, which means its smaller crossing size available to shrink device size, and their distributions are shown in Fig. 11.

We briefly estimate the area ratio *A* of parabolic crossing structure area to overall crossing dimension area (square 6 μm × 6 μm), which is defined:

$$A\,\% = (\text{ horizontal parabola area} + \text{vertical parabola area} - \text{overlap area})\,/36, \tag{5}$$

where parabola area = 4 × parabola area integral from $xx = -3$ to 0 μm, overlap area is a square. At right side, high transmission happens (> 97.5%) at $cc = -2.9$ μm, and its *A* is 53.07%; at left side, high transmission (>97.5%) in ranges of cc from −3.20 to −3.19 μm, and *A* from 35.15% to 35.53%. The *A* of partial parabolic single layer crossing is lower than double layer parabolic taper crossing about 18%. It means that the smaller dimension size of partial parabolic single layer be beneficial to shrink photonic circuits, and maybe it can contribute more areas for heat dissipation and system cooling.

The partial parabolic single layer crossing not only has high transmission, small size, low-loss and low crosstalk, but also high fabrication dimension tolerance. Even under ±10 nm dimension variation due to fabrication, it keeps high transmission

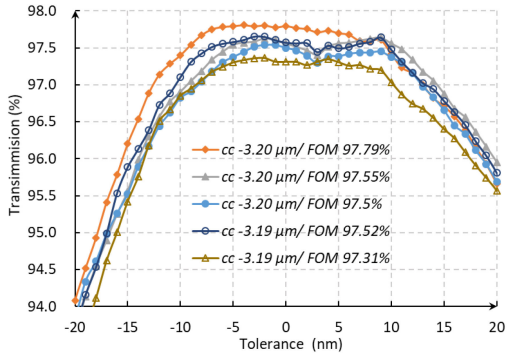

Fig. 12. Tolerance of partial parabolic single layer crossing.

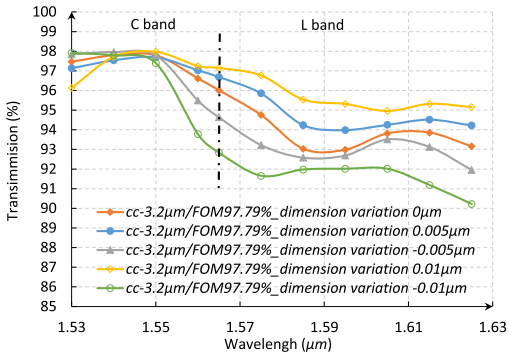

Fig. 13. FOM trends for the fabrication tolerance analysis in C+L band (1.530−1.625 μm).

TABLE IV
PERFORMANCE COMPARISON OF CROSSINGS

	Double layer parabolic taper crossing [12]	Double layer parabolic taper crossing (this work)	Partial parabolic single layer crossing (this work)
Transmission (%)	95-97.5	97.8	97.8
Crosstalk(dB)	-40	-66	-62
Number of structure layers	2	2	1
Area ratio A (%)	53.07	53.07	35.15−35.53

over 96.8%, details as shown in Fig. 12. Although the resolution of our device design is 0.0001 μm (0.1 nm) for the calculation and optimization, the transmission of the device can still be higher than 96.8% even the designed parameters are truncated into 0.01 μm (10 nm) according to the fabrication tolerance analysis. The minimum spacing between two devices of our design can be as small as 6 μm.

The FOM trends for the fabrication tolerance analysis in C+L band (1.530−1.625 μm) are shown in Fig. 13. Our device is basically designed at the wavelength of 1.550 μm, so the performance in C band is better than that in L band.

We compare the performances of the 3 kinds of crossings, including items of transmission, crosstalk, number of structure layers, and area ratio A as shown in Table IV.

III. CONCLUSION

We provide a partial parabolic single layer crossing, which has excellent performance of high transmission of 97.8% (−0.097 dB) and low crosstalk of −62 dB, which can simplify fabrication processes, reduce cost, and get narrower crossing to shrink device size to produce more compact photonic circuits, also keeping over 96.8% high transmission between ±10 nm fabrication dimension tolerance.

REFERENCES

[1] H. Nishihara, "Recent advancement on optical integrated circuits," in *Proc. Conf. Comput. Commun. Syst.*, 1990, pp. 99–103.
[2] A. V. Krishnamoorthy, "Photonics-to-electronics integration for optical interconnects in the early 21st century," *Optoelectron. Lett.*, vol. 2, pp. 163–168, 2006.
[3] B. Jalali and S. Fathpour, "Silicon photonics," *J. Lightw. Technol.*, vol. 24, no. 12, pp. 4600–4615, 2006.
[4] R. Soref, "The past, present, and future of silicon photonics," *IEEE J. Sel. Topics Quantum Electron.*, vol. 12, no. 6, pp. 1678–1687, Nov./Dec. 2006.
[5] M. Paniccia *et al.*, "A hybrid silicon laser: Silicon photonics technology for future tera-scale computing," *Technol.@Intel Mag.*, Oct. 2006.
[6] L. B. Soldano and E. C. M. Pennings, "Optical multi-mode interference devices based on self-imaging: Principles and applications," *J. Lightw. Technol.*, vol. 13, pp. 615–627, Apr. 1995.
[7] M. G. Daly, P. E. Jessop, and D. Yevick, "Crosstalk reduction in intersecting rib waveguides," *Lightw. Technol.*, vol. 14, pp. 1695–1698, 1996.
[8] H. Chen and A. W. Poon, "Low-loss multimode-interference-based crossings for silicon wire waveguides," *Photon. Technol. Lett.*, vol. 18, pp. 2260–2262, 2006.
[9] H. Liu, H. Tam, P. K. A. Wai, and E. Pun, "Low-loss waveguide crossing using a multimode interference structure," *Opt. Commun.*, vol. 241, pp. 99–104, 2004.
[10] T. Fukazawa, T. Hirano, F. Ohno, and T. Baba, "Low loss intersection of Si photonic wire waveguides," *Jpn. J. Appl. Phys.*, vol. 43, no. 2, pp. 646–647, 2004.
[11] C. Wei, F. Groen, M. Smit, I. Moerman, P. Van Daele, and R. Baets, "Integrated optical elliptic couplers: Modeling, design, and applications," *J. Lightw. Technol.*, vol. 15, pp. 906–912, May 1997.
[12] W. Bogaerts, P. Dumon, D. V. Thourhout, and R. Baets, "Compact, low-loss waveguide crossings for high-index-contrast SOI photonic wires," *Quantum Electron.*, vol. 12, pp. 1394–1396, 2006.
[13] W. Bogaerts, P. Dumon, D. V. Thourhout, and R. Baets, "Low-loss, low-crosstalk crossings for Silicon-on-Insulator nanophotonic waveguides," *Opt. Lett.*, vol. 32, pp. 2801–2803, 2007.
[14] D. M. Sullivan, *Electromagnetic Simulation Using The FDTD Method*. Hoboken, NJ, USA: Wiley, 2000.
[15] S. D. Gedney, "Introduction to the finite-difference time-domain (FDTD) method for electromagnetics," *Synth. Lectures Comput. Electromagn.*, vol. 6, no. 1, pp. 1–250, 2011.
[16] S. Dey and R. Mittra, "A locally conformal finite-difference time-domain (FDTD) algorithm for modeling three-dimensional perfectly conducting objects," *IEEE Microw. Guided Wave Lett.*, vol. 7, no. 9, pp. 273–275, Sep. 1997.
[17] S. Kiranyaz, T. Ince, and M. Gabbouj, *Multidimensional Particle Swarm Optimization for Machine Learning and Pattern Recognition*. Berlin, Germany: Spinger, 2014, pp. 70–75.
[18] R. Eberhart and J. Kennedy, "Particle swarm optimization," *Proc. IEEE Int. Conf. Neural Netw.*, vol. 4, Nov. 1995, pp. 1942–1948.
[19] Y. Shi and R. C. Eberhart, "Empirical study of particle swarm optimization," in *Proc. Congr. Evol. Computation-CEC99 (Cat. No. 99TH8406)* vol. 3, 1999, pp. 1945–1950.
[20] Y. Shi, "Particle swarm optimization: Developments, applications and resources," in *Proc. Congr. Evol. Computation (Cat. No. 01TH8546)*, IEEE, vol. 1, May 2001, pp. 81–86.
[21] W. H. Press, S. A. Teukolsky, W. J. Vetterling, and B. P. Flannery, *Numerical Recipes in C++, The Art of Scientific Computing*, 2nd ed. Cambridge, U.K.: Cambridge Univ. Press, 2002, pp. 353–400.